

# Mechanical and Transport Characteristics of Coal-Biomass Mixtures for Advanced IGCC Systems

Divya Chandra,<sup>\*,†</sup> Derek Elsworth,<sup>†</sup> and Dirk VanEssendelft<sup>‡</sup>

<sup>†</sup>Department of Energy and Mineral Engineering, EMS Energy Institute and G3 Center, Pennsylvania State University, University Park, Pennsylvania 16802-5000, United States

<sup>‡</sup>National Energy Technology Laboratory, 3610 Collins Ferry Road, P.O. Box 880, Morgantown, West Virginia 26507-0880, United States

**ABSTRACT:** We explore the relationship between mechanical, transport, and critical state characteristics of coal–biomass mixtures by evaluating mixture composition, stress, strength, rheology, and permeability of coal–biomass mixtures. We report measurements of strength and permeability evolution for uniformly graded (passing no. 200 mesh) granular mixtures of coal–biomass in the proportions (a) 100% sub-bituminous coal, (b) 75–25% sub-bituminous coal–biomass, and (c) 100% biomass. We observe response at confining stresses in the range 5 and 25 MPa and at strain rates of  $\sim 10^{-4}$ /s. The pure biomass is the most compliant and weakest of the three mixtures, and the coal is the stiffest and strongest. The samples stiffen with compaction as confining stress increases. Results show strain hardening for all sample mixtures resulting from grain breakage. Work hardening behavior is characterized using a CAP model. In all samples, permeability reduces with an increase in axial strain and yields permeabilities in the range  $10^{-14}$ – $10^{-16}$  m<sup>2</sup> (10–0.1 mD). We define the evolution of permeability as a function of changes in both porosity and grain breakage and link this to a model representing the harmonic mean of the particle diameters, as they evolve. This characterization works well and the harmonic mean of the particle size distribution is the best predictor of permeability evolution. These measurements are important in characterizing feed characteristics of dry-fed coal–biomass mixtures to prevent gas-flow back and to maintain feed rates into pressurized gasifiers.

## 1. INTRODUCTION

Increasing energy demand and advances in coal-gasification technology have changed the way we view coal. The use of coal is an inevitable option for power generation throughout the near future. Generation of electricity by integrated gasification combined cycle (IGCC) is one of the most versatile and clean methods to convert coal into electricity, hydrogen, and other valuable energy products. Rather than burning coal directly, gasification (a thermochemical process) converts the coal into its basic chemical constituents. In a modern gasifier, coal is typically exposed to steam and carefully controlled amounts of air or oxygen under high temperatures and pressures. This produces a mixture of carbon monoxide, hydrogen, and other gaseous compounds known as synthesis gas. The synthesis gas is typically cleaned by removing the flue gas contaminants prior to combustion in a gas turbine. IGCC systems are capable of significantly reducing discharge rates of all pollutants (solid, liquid, and gas) compared to conventional coal-fired systems.<sup>1</sup> Currently there are few commercial IGCC systems as they require significant investment and have high operating costs.<sup>2</sup> However, common to all large-scale gasification systems is the need for a method to feed ultradense-phase pulverized granular material into a high pressure reactor. One efficient approach to feeding the granular material is to feed it as an ultradense phase through a mechanical feeder known as a "lock bridge" feeder to reduce the void fraction which in turn eliminates the need for a carrier fluid.<sup>3</sup>

In order to achieve near-zero emissions, cofeeding biomass with coal is a promising option that may reduce net carbon output. Biomass is carbon neutral since it sequesters carbon

from the atmosphere until it is burnt. However some carbon is peripherally generated in its harvesting, preparation, and transportation. Biomass contains less sulfur and ash than coal. Therefore cofiring can result in decreased NO<sub>x</sub> and SO<sub>x</sub> emissions and also decrease the amount of solid waste generated.<sup>4</sup> The cocombustion of coal and biomass presents the opportunity to reduce net carbon emission over pure coal-firing by the inclusion of a carbon-neutral supplementary fuel-biomass. Key questions relate to how coal and biomass may be cofired using the current combustion plant. While lock hoppers exist and lock bridge feeders are being developed for coal, cofeeding biomass remains technically challenging and largely unaddressed. Biomass is a difficult material to handle and often creates blockages in hopper flows and can create plant stoppages. In most applications, this is undesirable, but for power applications, the requirement of a reliable and constant feed is critical. Utilization of coal–biomass mixtures in conventional plants requires that the granular mixture be fed continuously into the gasifier in a form close to the hard-coal form traditionally utilized. This may require that the coal–biomass mixture is preprocessed under compactive stress and/or temperature to improve its handling and gasification characteristics. For continuously fed compaction and gasification systems, the mechanical and transport properties of the mixture are key variables defining the ability to process the feed. The size and shape of the coal–biomass mixtures (feed)

Received: May 3, 2012

Revised: August 1, 2012



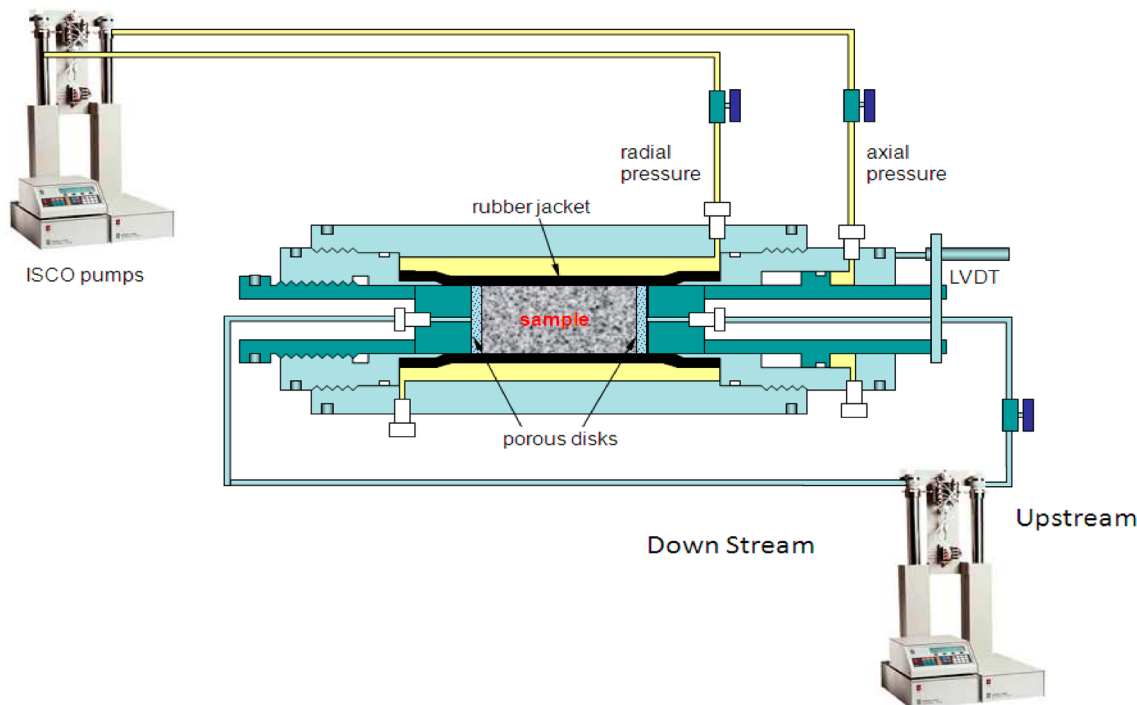


Figure 1. Schematic of the experimental apparatus.

influence their fluid flow and heat transfer characteristics.<sup>5</sup> Key relationships between material state (mixture composition, particle size, stress) and mechanical (frictional strength, rheology) and transport (permeability) characteristics are currently poorly defined. Determining these inter-relationships and upscaling anticipated behavior to prototype scale is the focus of this work.

The influence of elevated stresses on the deformation and fluid transmission properties of granular materials is a subject of traditional interest in soil mechanics. Studies of deformation in sandstones<sup>6–10</sup> and in sand<sup>11,12</sup> show cataclastic failure that results from grain crushing and pore collapse. Deformation and failure may be conveniently followed using critical state CAP models.<sup>7,8,11</sup> Permeability evolution is a function of stress path and consolidation state.<sup>13</sup> Significant permeability reduction is triggered by compaction caused both by loss of porosity and the onset of grain breakage.<sup>12,14</sup> Permeability–porosity relationships allow the parametrization for porous media. However, where grain breakage is significant, the inclusion of effects of pore occlusion by fugitive particles lodged within pore throats is an important additional feature that must be incorporated.

We present data from a series of low- to high-pressure laboratory experiments designed to explore the mechanical and transport characteristics of granular coal, biomass, and coal–biomass mixtures. Deformation experiments with continuous measurement of permeability are performed to failure under varied confining stresses for various mixtures of coal and biomass. We link the effects of compaction, confining stress, evolution of porosity, and comminution on permeability to define response in a mechanistically consistent manner.

## 2. EXPERIMENTAL TECHNIQUE

We use a standard triaxial apparatus to apply appropriate mean and deviatoric stresses at strain rates moderately consistent with the feed process. We concurrently measure deformation and permeability and infer from these measurements changes in porosity within the samples.

**2.1. Apparatus.** The system comprises a standard triaxial cell capable of accommodating cylindrical samples with stresses and fluid pressures applied by high pressure pumps (Figure 1). Samples of the loose granular coal, coal–biomass mixture or biomass are encased within a cylindrical heat-shrinkable poly olefin tube with porous metal frits allowing fluid transmission through the end platens. This assembly is second-jacketed by another heat-shrinkable poly olefin tube. Thus the sample is confined between the circular platens and plumbed to allow inflow and outflow of fluid. Inflow into and outflow from the sample is via rigid steel or flexible PTFE (polytetrafluoroethylene) piping. Flow within the inlet portion of the sample is distributed by a grooved flow-distributor. The confining stress is applied by a confining fluid—in this case water—pressurized by a single high-pressure pump. Axial stress or strain rate is applied by a second and independently controlled high-pressure pump. The apparatus is run in either stress or displacement control with stress-rates or displacement-rates independently managed by a data acquisition system (DAX: Labview). Fluids are circulated within the sample either by prescribed pressure or prescribed flow rate depending on the permeability of the material.

**2.1.1. Stress and Deformation Control System.** The mechanical response is modulated by control on applied stresses and complementary displacements and measured displacements or stresses.

**Confining Cell.** Samples representative of feed mixtures are loaded into the compression cell. Water as an incompressible fluid is used to apply radial confining stress to the sample and axial load is provided by an independent piston that compacts the sample in the longitudinal direction. The strain in the radial direction is measured by fluid volume displacement of the confining fluid and the strain in the axial direction is measured directly through a linear voltage distance transducer (LVDT). Samples are loaded to failure under conditions of prescribed stress rate or constant strain rate—the latter is used in the majority of experiments. During loading to failure, permeability is concurrently measured.

**Stress Control.** High pressure syringe pumps control confining stress, axial stress, and internal fluid pressure within the sample. Pump pressures may be applied in the range 1–70 MPa. These pumps are controlled via DAX and operate under stress or displacement control. Typically confining stress is stress controlled, axial loading is displacement controlled, and interior pressure is under volume or

pressure control, depending on whether permeability testing is transient or steady.

**Displacement Measurement.** With stresses applied to the sample, complementary displacements are measured. Axial (differential) strains and volume strains are measured as complementary measurements to the applied stresses. Axial strains are recorded by LVDT at a rate of 1 Hz. Volumetric strains are recovered from changes in volume of the confining fluid. Changes in the confining fluid volume, corrected for axial incursion of the end platens into the pressure cell enable the radial strains to be recovered, directly.

**2.1.2. Fluid Control System.** Fluid control is applied to the sample to (i) control the magnitude of applied fluid pressures and therefore effective stresses and (ii) to measure permeability of the sample. Two modes of permeability measurement are feasible. These are (i) steady-state flow-through experiments and (ii) transient pulse permeability measurements. The steady measurements are preferable as they give a time-continuous measurement of permeability but are difficult to maintain where internal deformations within the sample are rapid, and corrections must be applied. The external arrangements for each measurement differ.

Steady measurements of permeability are recovered from end-to-end through-flow experiments on the sample. Upstream fluid pressures are set, and the downstream fluid discharges through the platen at atmospheric pressure or under a prescribed backpressure. Measured volumetric flow-through at prescribed pressure drop enables permeability to be recovered from Darcy's law. Where deformation of the sample is significant, the flow-through flux must be corrected for the undrained volume change. The arrangement for flow-through measurements is shown in Figure 1.

**2.1.3. Grain Size Density.** Grain density of samples is measured using a multipycnometer that measures the pressure difference resulting when a known quantity of helium gas under pressure is allowed to flow from a precisely known reference volume into a sample cell containing the granular sample.

**2.1.4. Particle Size Distribution.** Particle size distribution (PSD) measurements are completed on undeformed (pretest) and deformed (post-test comminuted) granular samples using laser diffraction. A particle size distribution is calculated from measurements of the angular intensity of scattered light produced by a dispersed sample. Ethanol is used as a solvent to achieve better dispersion of the powdered coal and to obtain accurate results. Particles are collected from the center (failure plane) of the samples.

**2.2. Experimental Procedure.** Confining stresses and internal fluid pressures are applied to the cylindrical granular sample. Axial loads develop as a consequence of constant displacement velocity of the axial platen, applied as a result of constant injection rate from the axial loading pump. Responses to these applied conditions are measured through the complementary measurements of radial displacement of the sample (volume change of the confining fluid), shortening of the sample (via LVDT) and flow rate through the sample (via pump). These measurements are recovered to define the mechanical (rheological and strength) and transport behavior of the granular mixtures. The final porosity is calculated by knowing the water content (ratio of the masses of water and of dry sample) and grain density, and change in porosity is tracked by following the volume change of confining fluid during the experiment.

**2.2.1. Mechanical Behavior.** Samples are tested as cylindrical specimens with flat ends confined between rigid end-platens and sheathed in an impermeable but flexible membrane. Initial conditions comprise stresses elevated to a predetermined isotropic magnitude with axial compression increased until failure while the resisting stress is recorded with axial strain. Failure is typically defined as a peak in the deviatoric stress (maximum axial stress minus the minimum radial stress) or for work hardening materials as a stress at a prescribed axial strain. Maximum principal stress magnitudes at failure for samples confined at a range of minimum principal stresses (confining stress) are used to determine shear strength for a maximum shear stress to normal stress ratio evaluated on the failure plane (Mohr Coulomb). For samples where the radial stresses represent a single magnitude such that the minimum and intermediate principal stresses are equal,

failure stress is independent of the intermediate principal stress. Measurements of strength may be in error by only 5–10% for this simplifying assumption,<sup>15</sup> but similar trends in strength with strain rate, material composition, and material gradation will still apply. This small error is more than warranted given the significantly simplified experimental procedure and the ability to complete multiple repeat experiments in lieu of the more complex experimental arrangement for which the Temco cell is incapable of following the correct stress path.

**Axial Volumetric and Radial Strains.** The evolution of strain is recovered from the concurrent measurement of axial shortening and diametric widening. Axial shortening is measured directly by LVDT. Radial strain is inferred from the volume change of the sample recovered from the volume change in the confining fluid under constant confining pressures—appropriately corrected for axial displacements of the end platens.

Axial strain is recovered directly from the change in length,  $\Delta l$  over a reference length,  $l$ , as

$$\epsilon_a = \frac{\Delta l}{l} \quad (1)$$

Volumetric strain is recovered from the measured change in volume of the confining fluid  $\Delta V_3$  under constant pressure. Since the fluid is at constant pressure, the change in volume of the sleeve that jackets the sample is negligible, despite the change in deformation of the sample. The volume of the confining fluid is corrected by subtracting the volume change due to the movement of the piston into the confining cell. Volumetric strain is given by

$$\epsilon_v = \frac{\Delta V_3}{V_s} \quad (2)$$

Where  $\epsilon_v$  is the volumetric strain measured for a volume change of the confining fluid  $\Delta V_3$  over the volume of the sample  $V_s$ .

Radial strain is recovered as

$$\epsilon_r = \frac{\epsilon_v - \epsilon_a}{2} \quad (3)$$

Strains are measured as a consequence of the applied stresses. Compressive stress and compactive axial and volumetric strains are taken to be positive. Differential stress (which is also known as deviatoric stress) is defined as the difference between the axial stress and confining stress.

$$q = \sigma_1 - \sigma_3 \quad (4)$$

Effective mean stress is defined as

$$p' = \left( \frac{(\sigma_1 - p_u) + 2(\sigma_3 - p_u)}{3} \right) \quad (5)$$

where,  $\sigma_1$  = axial stress,  $\sigma_2 = \sigma_3$  = confining stress, and  $p_u$  is the pressure of the pore fluid.

**2.2.2. Transport Behavior.** Permeability is a measure of an ability of fluids to flow through a medium under the action of a pressure gradient. Permeability is affected by the (i) presence of air bubbles, (ii) degree of saturation, (iii) effective grain size, (iv) tortuosity, (v) pore pressure, (vi) confining stress, (vii) grain size distribution, and (viii) grain shape.<sup>16</sup> Permeability can be recovered from the steady measurements of flow-through rate under constant pressure drop provided flow corrections are applied for undrained changes in volume of the sample.

**Steady State Measurements.** Permeability  $k$  may be measured for a slightly compressible fluid of known viscosity  $\mu$  discharging across the sample of length  $\partial x$  at a prescribed pressure drop  $\partial p$ . The volumetric flow rate  $q_x$  discharging across the sample is incorporated in Darcy's law as

$$q_x = \frac{-k}{\mu} \frac{\partial p}{\partial x} \quad (6)$$

However, this flow rate is uncorrected for concurrent volume changes that occur within the sample as a result of compaction or dilation.

These volume changes may be corrected for in the sample by considering the effect of volume change as

$$q_x = \frac{-k}{\mu} \frac{\partial p}{\partial x} + \dot{\epsilon} dx \tag{7}$$

Where,  $\dot{\epsilon}$  is volumetric strain rate. The influence of compaction of the sample due to applied strain rate may be determined by decomposing the problem into two parts. These are (i) the flow of fluid induced by compaction of the sample and (ii) that driven by the applied pressure gradient.

(i) *Flow Induced by Applied Strain Rate.* A uniform strain rate is applied throughout the sample and expels fluid from the sample as a result of compaction. Fluid flows to either end of the sample (Figure 2) and a nonuniform distribution of pressure gradient will develop, centered at the center of the sample (Figure 2).

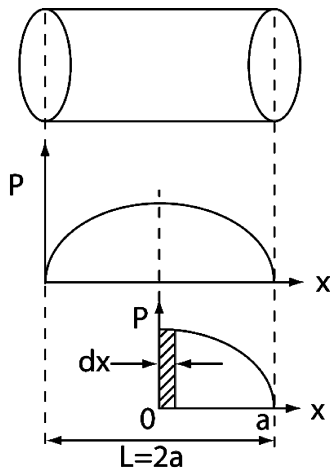


Figure 2. Pore pressure distribution profile inside the sample during uniform applied external strain rate.

At the center of the sample the flux across the  $x = 0$  boundary is null requiring that the pressure gradient is also zero (Figure 2). The continuity condition for steady flow is

$$\frac{\partial q_x}{\partial x} = 0 \tag{8}$$

and substituting eq 8 yields

$$0 = \iiint \left( \frac{-k}{\mu} \frac{\partial^2 p}{\partial x^2} + \dot{\epsilon} \frac{\partial}{\partial x} (dx) \right) \tag{9}$$

or

$$0 = \frac{-k}{\mu} p + \dot{\epsilon} \frac{x^2}{2} + c \tag{10}$$

Where  $c$  is an integration constant. With the requirement that  $p = 0$  at  $x = \pm a$  (Figure 2), then the integration constant may be evaluated as

$$c = \frac{-\dot{\epsilon} a^2}{2} \tag{11}$$

Substituting eq 11 into eq 10, we obtain

$$p = \frac{\mu \dot{\epsilon}}{2k} (x^2 - a^2) \tag{12}$$

defining the parabolic distribution of pressure along the length of the sample.

(ii) *Flow Induced by Uniform Pressure Gradient.* The parabolic distribution of pressure resulting from uniform compaction of the sample is superposed on the steady flow condition within the sample. The linear pressure distribution (Figure 3) may be superposed on the

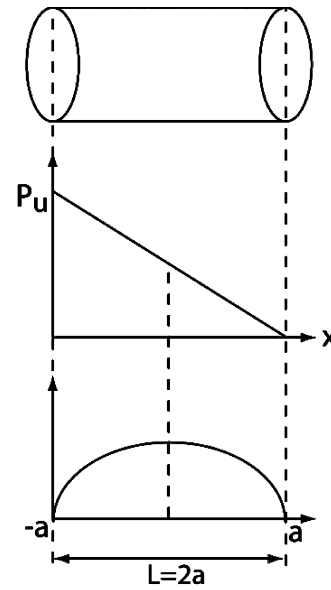


Figure 3. Combined pore pressure distribution due to steady longitudinal flow and due to compaction.

pressure distribution due to compaction. The overall pressure distribution along the sample due to prescribed upstream and downstream pressure conditions is

$$p = \frac{p_u}{2} \left( 1 - \frac{x}{a} \right) \tag{13}$$

where  $p_u$  is the pore pressure drop along the sample of length  $2a$ .

Combining eqs 12 and 13 enables the overall pressure distribution to be defined by superposition as

$$p = \frac{p_u}{2} \left( 1 - \frac{x}{a} \right) + \frac{\mu \dot{\epsilon}}{2k} (x^2 - a^2) \tag{14}$$

and

$$\frac{dp}{dx} = -\frac{p_u}{2a} + \frac{\mu \dot{\epsilon}}{k} \tag{15}$$

From Darcy's law the volumetric flow rate  $Q_x$  for the ends of the sample can be defined as

$$Q_x = -A \frac{k}{\mu} \frac{dp}{dx} \Big|_{x=\pm a} \tag{16}$$

Substituting eq 15 into 16 yields

$$k = \frac{\mu L}{p_u} \left( \frac{Q_x}{A} + \frac{\dot{\epsilon} L}{2} \right) \tag{17}$$

Thus eq 17 enables the steady state permeability of the sample to be determined by considering the effect of volume change of the sample during the experiment where  $A$  is the cross sectional area of a sample. This is used to reduce the data in the experiments reported later in this work.

### 3. EXPERIMENTAL OBSERVATIONS

A suite of experiments is completed to explore the role of coal–biomass mixture proportions on the evolution of rheological and transport properties. The mixtures are 100% coal, 75% coal/25% biomass, and 100% biomass as summarized in Table 1. We present results from experiments performed under both nonhydrostatic and hydrostatic (isotropic) loading conditions. We discuss mechanisms of deformation and their influence on transport behavior with material properties defined in Table 2.

**Table 1. List of Experiments and Corresponding Conditions**

experiment	coal (%)	biomass (%)	axial strain rate (1/s)	pore fluid	confining stress (MPa)
1	100	0	$10^{-4}$	water	5
2	100	0	$10^{-4}$	water	25
3	75	25	$10^{-4}$	water	5
4	75	25	$10^{-4}$	water	25
5	0	100	$10^{-4}$	water	5
6	0	100	$10^{-4}$	water	25
7	100	0	$10^{-4}$	water	isotropic loading
8	75	25	$10^{-4}$	water	isotropic loading
9	0	100	$10^{-4}$	water	isotropic loading
Ps1	100	0	$10^{-4}$	water	5
Ps2	100	0	$10^{-4}$	water	5
Ps3	100	0	$10^{-4}$	water	5

**Table 2. Material Properties**

properties	
viscosity of water (Ns/m <sup>2</sup> )	$1.002 \times 10^{-3}$
specific gravity of 200 mesh sub-bituminous coal	1.326
specific gravity of 200 mesh sub-bituminous coal–biomass mixture(75:25)	1.396
specific gravity of 200 mesh biomass	1.465

**3.1. Mechanical Response.** We examine the mechanical and transport characteristics of the various mixtures in triaxial compression under constant applied confining stresses of 5 and 25 MPa as a representative range of loading conditions. The strain produced during the initial hydrostatic loading is disregarded. The differential stress–strain data represent compressive axial strain and expansive radial strain and are different between the coal, coal–biomass, and biomass samples. The strains (axial and radial) produced in the coal are the smallest and are largest in the pure biomass (Figure 4). The

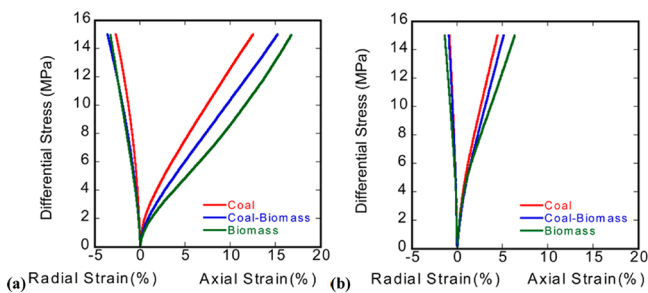


**Figure 4.** Comparison of the differential stress as a function of axial and radial strain for (i) coal, (ii) coal–biomass mixture, and (iii) biomass samples for constant applied confining stress at (a) 5 and (b) 25 MPa.

steepness of the samples (slope of stress–strain curves) increases for coal, coal–biomass mixtures, and biomass with increasing confining stress. The magnitude of strains (axial and radial) decrease in all sample types at the higher confining stress of 25 MPa. Compaction continues during deviatoric loading in all experiments. Because of strain hardening, steady states are not reached at least to an applied deviatoric stress of 15 MPa.

**3.1.1. Effective Mean Stress.** Additional insights are gained by plotting porosity and volumetric strain as a function of effective mean stress (Figure 5). All samples subjected to constant pore pressure of 1 MPa show relatively similar

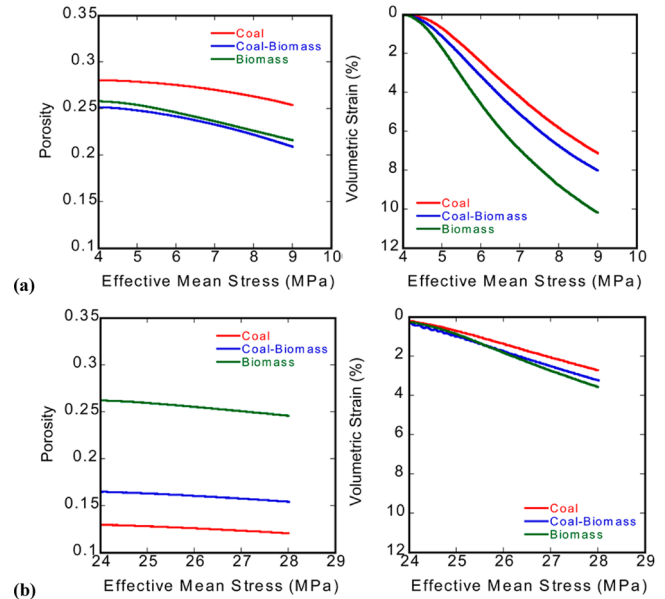


**Figure 5.** Comparison of porosity and volumetric strain as a function of effective mean stress for (i) coal, (ii) coal–biomass mixture, and (iii) biomass samples for constant applied confining stress at (a) 5 and (b) 25 MPa.

behavior—i.e., a decrease in porosity with an increase in effective mean stress. Change in porosity during the initial hydrostatic loading is disregarded. The strength of all samples is insensitive to their porosities. Decreasing porosity indicates compaction with most of the samples (coal, coal–biomass, and biomass) in the porosity range 20–30%. Porosity reduction is higher for low applied confining stress (5 MPa) compared to the higher confining stress of 25 MPa. Porosity reduction for the samples decreases with an increase in the confining stress. For low confining stress (5 MPa), a 4–5% reduction in porosity is observed compared to a 2–3% porosity reduction at high confining stresses (25 MPa).

The volumetric strain increases linearly with an increase in the effective mean stress. A large volumetric strain is produced at a constant applied low confining stress of 5 MPa. The compactive volumetric strain produced in the biomass is largest and is least in the coal samples at constant applied low and high confining stresses. All specimens demonstrate compaction and work hardening at low and high confining stresses.

**3.1.2. Hydrostatic Stress.** Hydrostatic constant strain rate experiments are conducted to determine the critical strength of the samples. Figure 6 illustrates a comparison of effective stress versus volumetric strain for the three samples at constant applied pore pressure of 1 MPa. All samples compact but at different compaction rates as effective mean stress is increased. The inflection point of the linear effective stress–volumetric strain curve defines the critical effective pressure for the onset of grain breakage. Critical strength of all the three sample types is less than 1 MPa (Figure 6). This indicates that grain breakage begins in the very early stages of hydrostatic loading with coal having the highest critical strength and biomass the least.

**3.2. Strain Envelope.** The strain envelope may be defined by prescribing failure strains within the samples. The contours for mean and deviatoric stresses at 20% strain are shown in Figure 7 ( $p'$ – $q$  stress space). Under triaxial compression, the sample is loaded hydrostatically until the desired confining stress of either (a) 5 MPa or (b) 25 MPa, followed by the

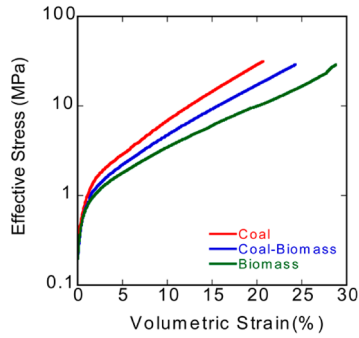


**Figure 6.** Comparison of the effective stress as a function of volumetric strain for (i) coal, (ii) coal–biomass mixture, and (iii) biomass samples for constant applied pore pressure at 1 MPa, under hydrostatic loading condition.

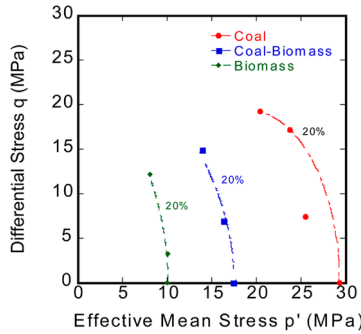


**Figure 7.** Comparison of the elliptical envelope of 20% volumetric strains in  $p'$ – $q$  space for (i) coal, (ii) coal–biomass mixture, and (iii) biomass samples.

application of a deviatoric stress of 15 MPa by increasing the axial stress. The effective mean stress and deviatoric stress path increases at a slope of 3:1. The strain developed during initial hydrostatic loading is taken into consideration. The important observations are (i) as the critical strength of the samples for grain crushing is less than 1 MPa (Figure 6), the strain contours for the samples represent composite effects of compaction and grain crushing, (ii) the equivalent strain envelope for the coal occurs at elevated stresses approximately three times larger than for the biomass, and (iii) the strain contours for the biomass are steep in comparison to those for the coal–biomass mixture and coal.

**3.3. Transport Response.** Axial permeabilities recovered from the experiments are plotted as a function of axial strain (Figure 8). Permeability is measured only during deviatoric loading but for all experiments. The important feature is that permeability consistently decreases with an increase in axial strain for all samples at both low and high applied confining stress. The permeability of the biomass alone is the lower than for coal or coal–biomass mixtures. The rate of permeability reduction increases with an increase in confining stress. This indicates that permeability is more strongly controlled by confining stress. The rate of permeability reduction is largest in the coal at both low and high confining stress.

**3.3.1. Porosity.** Permeability and porosity are measured independently in all experiments. Permeability reduces in all samples with an increase in confining stress and with a concomitant decrease in porosity. The porosity–permeability relationship shows the linear trend and can be represented by a power law (Figure 9).

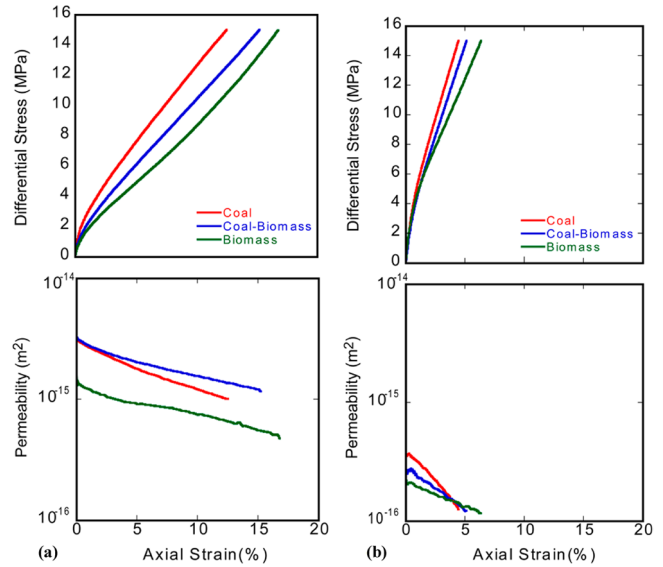


**Figure 8.** Comparison of the differential stress and permeability as a function of axial strain for (i) coal, (ii) coal–biomass, and (iii) biomass samples for constant applied confining stress of (a) 5 and (b) 25 MPa.

$$\log\left(\frac{k}{k_0}\right) = \log\left(\frac{n}{n_0}\right)^\alpha \quad (18)$$

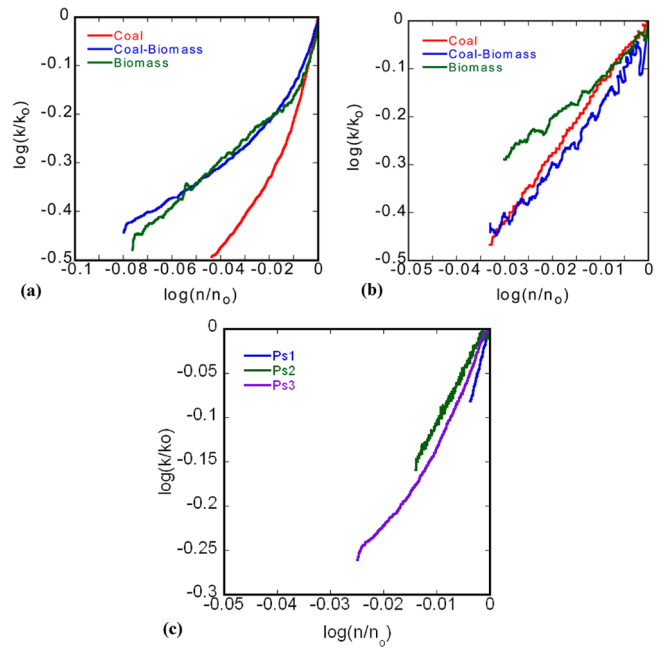


**Figure 9.** Comparison of the permeability ratio as a function of porosity ratio for coal, coal–biomass mixture, and biomass for constant applied confining stress at (a) 5 and (b) 25 MPa. (c) Comparison of the permeability ratio as a function of porosity ratio for coal for constant applied confining stress at 5 MPa.

where  $k$  = final permeability,  $k_0$  = initial permeability,  $n$  = final porosity, and  $n_0$  = initial porosity. An uncharacteristically large reduction in permeability is observed with an increase in the differential stress and with only a small loss in porosity. This results in large magnitudes of the exponent  $\alpha$  as illustrated in Table 3. The magnitudes of this exponent should be  $\alpha = 3$  for a compacting medium but the magnitudes noted in Table 3 are

**Table 3. Permeability Sensitivity of the Porosity Exponent ( $\alpha$ ) for Different Experiments**

experiment	constant confining stress (MPa)	differential stress (MPa)	$\alpha$
1	5	15	10.94
2	25	15	14.14
3	5	15	4.87
4	25	15	12.81
5	5	15	4.96
6	25	15	8.8
Ps1	5	0	22.85
Ps2	5	5	11.89
Ps3	5	10	10.88

in the range 5–23. This disparity is believed due to the occurrence of grain breakage and clogging and is explored in the following section.

**3.4. Microstructural Observations.** Grain size distribution of both undeformed and deformed samples of coal subjected to a confining stress of 5 MPa and differential stresses of (i) 0 MPa (Ps1,  $\sigma_1 = 5$  MPa), (ii) 5 MPa (Ps2,  $\sigma_1 = 10$  MPa), and (iii) 10 MPa (Ps3,  $\sigma_1 = 15$  MPa) evolve differently as identified in Figure 10. The peak abundance decreased in grain

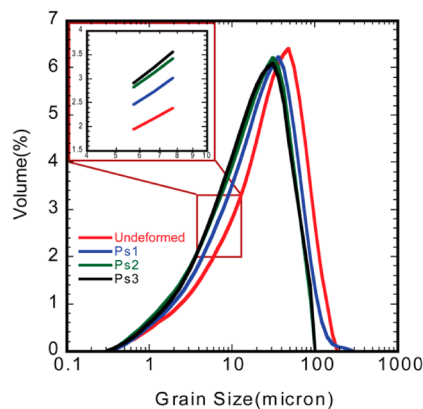


**Figure 10.** Comparison of the grain size distribution of (i) undeformed coal and (ii) deformed coal at the applied constant confining stress of 5 MPa (a) Ps1 sample, (b) Ps2 sample, and (c) Ps3 sample.

size, and the volume of fine particles increased with an increase in differential stress. The pre- and post-test measurements of grain size distribution of the samples (Ps1, Ps2, and Ps3) confirm the presence of grain breakage as a potential contributor to the high sensitivity of permeability to deviatoric stress.

## 4. DISCUSSION

From the experimental observations, certain trends are apparent in the mechanical and transport behavior of all samples. Microstructural evidence suggests that the small amount of grain breakage that results in the experiments exerts disproportionate impacts on the deformation and transport response. We analyze general trends in response and provide mechanistic models to represent behavior.

**4.1. Mechanical Response.** All stress paths followed in the experiments result in strain hardening where the deformation is apparently dominated by compaction. Higher strain rates also affect the strength and the stiffness of the sample. The critical

strength of all samples is found to be less than  $\sim 1$  MPa (Figure 5), so grain breakage is initiated even for an initial hydrostatic loading. Thus this initiates early in the compaction loading of all samples and continues over the full range of axial (deviatoric) loading. This is manifest in the grain size distribution data—the volume of fine grains increases in the deformed samples (Figure 10). The reduction in porosity with an increment of the effective mean stress is less at high confining stresses as the generation of fine particles is concomitantly increased. Pore throats are more effectively occluded by comminuted particles than by compactive reduction in porosity.<sup>10</sup>

**4.2. Work Hardening Model.** Strain hardening is ubiquitous for all the triaxial compression experiments. Strain hardening behavior is primarily due to grain crushing which start to occur in the early stages of the loading path (mean stress  $\sim 1$  MPa) and especially for high axial strain rates. Grain breakage and pore collapse promotes strain hardening.<sup>10</sup> Granulation results in the formation of finer particles that are stronger than the coarser particles that remain.<sup>17</sup> Strain hardening is affected by confining stress and strain rate.<sup>18</sup> For the triaxial deformation experiments, volumetric strain data of all sample types define an elliptical envelope consistent with hardening (CAP) models from critical state soil mechanics. We model volumetric strain data using a parametric equations for an elliptical failure envelope as<sup>8</sup>

$$\frac{(p'/H^* - M_1)^2}{(1 - M_1)^2} + \frac{(q/H^*)^2}{M_2^2} = 1 \quad (19)$$

where,  $p'$  = effective mean stress (MPa) (deviatoric experiments),  $H^*$  = effective mean stress (MPa) (hydrostatic experiments),  $M_1 = 0.5$ ,  $M_2 = 0.5-0.7$ , and  $Q$  = differential stress (MPa).

In the compaction regime, strain envelopes expand with decreasing grain size and decreasing porosity. Strain caps for all sample types illustrate plastic hardening. For all sample types, observations resemble previous studies on granular quartz sands,<sup>11</sup> carbonates,<sup>7</sup> and sandstone<sup>6,8</sup> in terms of strain and porosity. In the post failure regime, the strain contours become nonlinear (Figure 7). Overall, these contours of volumetric strains map the stress induced deformation of coal–biomass mixtures.

**4.3. Transport Response.** Compaction and grain breakage has a significant influence on permeability for all the experiments—permeability reduction is observed under axial loading in all experiments. Cataclastic deformation is effective in reducing permeability.<sup>12</sup> Pore collapse, the mobilization of granular debris filling the pore space, and the resulting clogging of pore throats are common features for the samples tested at higher effective stresses—in particular above the critical stress which results in the loss of permeability.<sup>19</sup> The changes in permeability are not related to porosity change because of the ability of granular debris to clog pore-fluid channels and inhibit flow.<sup>12</sup> Grain crushing and the formation of microcracks in grains changes the flow tortuosity which also affects the permeability. A drastic decrease in pore size and increase in microcrack density occurs in the grains which are deformed beyond the yield point. This lowers the local hydraulic conductance of individual pore channels and increases the tortuosity of the connected pore space resulting in an overall decrease in permeability.<sup>9</sup>

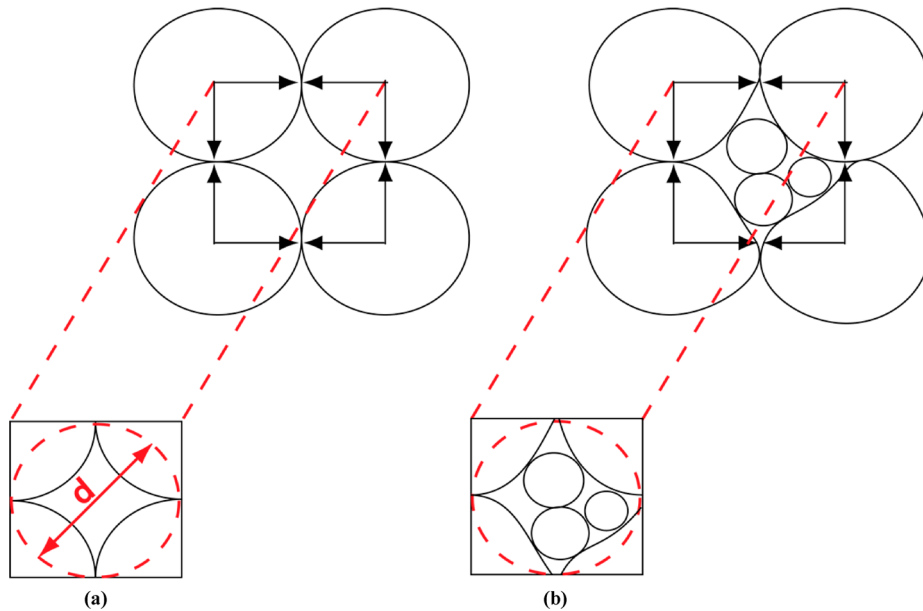


**Figure 11.** Schematic diagram (a) showing single capillary tube formation by arrangement of spherical grains and (b) showing capillary tube occlusion due to grain breakage.

**4.4. Evolution of Permeability.** We explain the anomalous permeability results by scaling with the Kozeny–Carman permeability–porosity model.

$$\frac{k}{k_0} = \left( \frac{n}{n_0} \right)^\alpha \quad (20)$$

where  $k$  = final permeability,  $k_0$  = initial permeability,  $n$  = final porosity,  $n_0$  = initial porosity, and  $\alpha = 3$

The Kozeny–Carman permeability–porosity model gives a poor prediction of permeability evolution for all the experiments reported here as the value of the exponent  $\alpha$  is shown to be considerably greater than three (Table 3). Similar outcomes are observed for crushed gravel sands<sup>20</sup> and for sandstones stressed beyond the critical stress at which grain crushing occurs.<sup>19</sup> The inability of the Kozeny–Carman model to effectively evaluate changes in permeability in these conditions may result from the assumption that the particle size distribution is invariant.<sup>21</sup> The Kozeny–Carman model assumes that the grain size distribution and related capillary distribution is both uniform and invariant (Figure 11). However, this is not the case for the coal biomass mixtures described here (Figure 10). In these experiments grain breakage contributes to a small but measurable change in the finest portion of the grain size distribution. We speculate that these fine particles are mechanically trapped in the pore throats where they occlude flow. This accumulation, specifically in pore throats, would have a large impact on permeability but may occur for no net change in porosity—hence the anticipated high sensitivity of permeability to grain comminution and low sensitivity to change in porosity.

**4.4.1. Permeability–Porosity Model.** We develop a rational method to predict changes in permeability from grain comminution based on a Kozeny–Carman model which includes the effect of grain breakage. We support this with the permeability, porosity, and grain size distribution data presented in this paper.

The general expression for permeability based on the Kozeny–Carman model is

$$k \propto \frac{n^\alpha}{(1-n)^2} d^2 \quad (21)$$

where,  $k$  is permeability,  $n$  is porosity,  $\alpha = 3$ , and  $d$  is grain diameter.

Since porosity is typically much smaller than unity, then the term  $n^\alpha/(1-n)^2$  is dominated by the term  $n^\alpha$ . Therefore, comparing the permeability,  $k$ , to the initial permeability,  $k_0$ , then from eq 21

$$\frac{k}{k_0} = \left( \frac{n}{n_0} \right)^\alpha \left( \frac{d}{d_0} \right)^2 \quad (22)$$

which may be represented as

$$\log \left( \frac{k}{k_0} \right) = \alpha \log \left( \frac{n}{n_0} \right) + 2 \log \left( \frac{d}{d_0} \right) \quad (23)$$

Assuming that grain diameter and porosity follow a power law relationship, since a reduction in porosity would result in a reduction in grain diameter, then

$$\left( \frac{d}{d_0} \right) = A \left( \frac{n}{n_0} \right)^\beta \quad (24)$$

where,  $A$  is a constant,  $\beta$  is a porosity exponent representing the change in grain diameter,  $d_0$  is initial grain diameter, and  $d$  is final grain diameter.

Substituting eq 24 into 23, we obtain

$$\log \left( \frac{k}{k_0} \right) = \alpha \log \left( \frac{n}{n_0} \right) + 2 \log \left[ A \left( \frac{n}{n_0} \right)^\beta \right] \quad (25)$$

or

$$\log \left( \frac{k}{k_0} \right) = (\alpha + 2\beta) \log \left( \frac{n}{n_0} \right) + 2 \log A \quad (26)$$

Neglecting the constant  $A$  that represents an offset in log–log space, we determine that

$$\log\left(\frac{k}{k_o}\right) \propto \alpha' \log\left(\frac{n}{n_o}\right) \tag{27}$$

where  $\alpha' = \alpha + 2\beta$

Equation 27 gives a new permeability–porosity model that links change in permeability to the combined influence of changes in porosity and changes in grain size distribution.

**Porosity–Grain Size Relationship.** With the current apparatus, it is not possible to measure the continuous change in grain size and relate it with the change in porosity during the experiment. However a linear relationship is assumed between the grain size and the porosity of the sample.  $\beta$  is obtained by plotting the ratio of the final and initial grain diameter as a function of the ratio of the final and initial porosity (Figure 13).

**Means of Particle Size Distributions.** The particle size distribution can be described using different means on volume, surface, length, or number, and these can be related to different features or behaviors. In this study, the grain size distribution is obtained using a laser diffraction technique and is based on volume. However a general expression for the different means of the particle size distribution can be obtained by the following eq 28<sup>22</sup>

$$D[m, n] = \left[ \frac{\sum d_i^{m-3} V_i}{\sum d_i^{n-3} V_i} \right]^{1/(m-n)} \tag{28}$$

where  $V_i$  is the relative volume of particles of diameter  $d_i$  and  $m$  and  $n$  are integer values that describe the mean being used. Two different mean sizes are used in this study. They are (i) the  $d_{32}$  or  $D[3, 2]$  (Sauter mean or harmonic mean size) and (ii) the  $d_{31}$  or  $D[3, 1]$  (volume mean size).

(i) **Harmonic Mean Grain Size.** Comminution of the grains results in a variation in the grain size distribution inside the sample which shows a significant effect on the permeability. Pressure gradient is one of the defining factors for the permeability of a porous medium. Under applied stresses, the particles will comminute and produce fines which will be mobile within the sample. Where these particles are mechanically strained in the pore throats, they will occlude flow. We consider two bounding arrangements of the coarse-through-fine particles comprising the sample, relative to the direction of forced fluid flow (Figure 12). These are with flow either parallel or perpendicular to the resulting segregated layering of the particulates. For this arrangement, the end-member permeabilities for layer-parallel (parallel flow) and layer-normal (series flow) are bounded by the arithmetic and harmonic means of the local permeabilities.<sup>23–25</sup> In this case, the change in permeability with comminution is observed to be so large that we presume it is principally related to the series flow and hence the harmonic mean. Thus we use the weighted harmonic mean grain size to calculate the porosity exponent of grain diameter ( $\beta$ ) by considering series flow for all our flow-through experiments (Figure 14).

From the grain size distribution data, the weighted harmonic mean of the grain sizes is calculated by

$$d_{32} = \frac{\sum V_i}{\sum \frac{V_i}{d_i}} \tag{29}$$

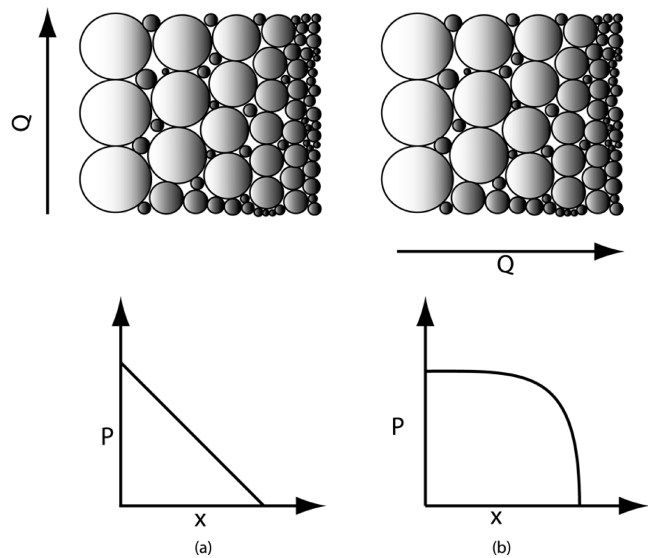


Figure 12. Pressure gradient during (a) series flow to the medium and (b) parallel flow to the medium.

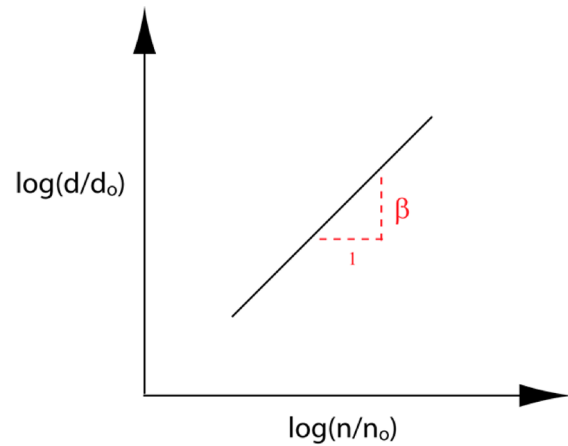


Figure 13. Schematic model relating grain diameter and porosity.

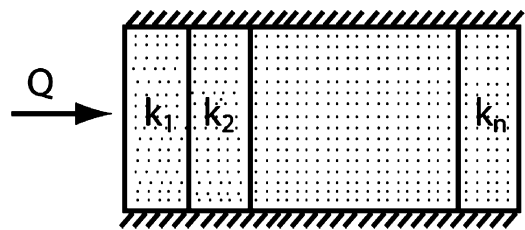


Figure 14. Flow normal to layers in a confined porous medium.<sup>26</sup>

Where  $d_{32}$  = weighted harmonic mean grain size,  $V_i$  = percent volume of the grain size, and  $d_i$  = grain size

(ii) **Volume Mean Grain Size.** The volume mean size is commonly used in two phase flows of bulk solids as it represent the control-volume averaged body force vector for the fluid–solids gradient term.<sup>3</sup>

The volume mean of the grain sizes is calculated by

$$d_{31} = \left[ \frac{\sum V_i}{\sum \frac{V_i}{d_i^2}} \right]^{1/2} \tag{30}$$

where  $d_{31}$  = volume mean grain size,  $V_i$  = percent volume of the grain size, and  $d_i$  = grain size.

Grain diameters obtained from the weighted harmonic mean and from the volume mean of the particle size distribution are plotted as a function of porosity (Figure 15). The  $\beta$  values obtained are used to calculate the permeability using the proposed model.

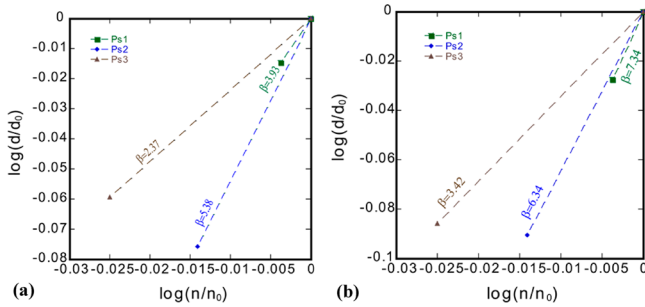


**Figure 15.** Grain diameter as a function of porosity for experiments (i) Ps1, (ii) Ps2, and (iii) Ps3. The grain diameters used are obtained from both (a) the volume mean size ( $d_{31}$ ) and (b) the harmonic mean size ( $d_{32}$ ) of the particle size distribution.

**Model Results.** Comparison of the Kozeny–Carman model, measured, and calculated ratio of final and initial permeability using the proposed model for volume mean ( $d_{31}$ ) and harmonic mean ( $d_{32}$ ) grain size are plotted as a function of axial strain for triaxial compression experiments on coal with a constant applied confining stress of 5 MPa and axial stresses of (i) 5, (ii) 10, and (iii) 15 MPa (Figure 16). The Kozeny–Carman model gives improper permeability prediction for all different experiments. A systematic trend is evident that with an increase in axial strain due to increasing axial stress results in a reduction in measured as well as calculated permeability ratio. At zero deviatoric stress, the trend of the measured permeability ratio is similar to the permeability ratio calculated from the proposed

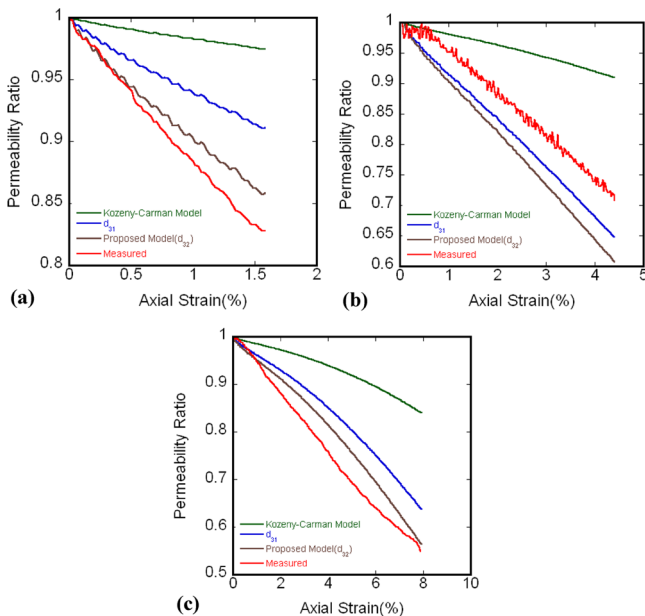


**Figure 16.** Comparison of the permeability ratio as a function of axial strain with the model fits using volume mean size ( $d_{31}$ ) and harmonic mean ( $d_{32}$ ) grain sizes for experiments (a) Ps1, (b) Ps2, and (c) Ps3.

model using different mean sizes; however, the harmonic mean grain size ( $d_{32}$ ) gives a better match (Figure 16a). This is because the harmonic mean better represents the physics of the permeability transformation. Where comminuted portions of particles are washed downstream and fill the interstices of the pore network, the permeability distribution becomes locally a series flow system. The bulk permeability of this series layered system results is rigorously identified by the harmonic mean of the local permeabilities—hence the improved fit relative to other means (such as the Sauter mean). The curves of the measured and calculated permeability ratio differ slightly at completion of the experiment because of the difference magnitudes of  $\alpha'$ . At a deviatoric stress of 5 MPa, the permeability ratio calculated using the proposed model does not match the permeability ratio obtained experimentally. The proposed model overpredicts the permeability change during the deformation for both volume mean and harmonic mean grain size (Figure 16b). At a deviatoric stress of 10 MPa, the measured permeability ratio initially matches the permeability ratio obtained from the model but later differs due to the difference in  $\alpha'$  (Figure 16c).

## 5. CONCLUSIONS

We investigate the mechanical and transport characteristics of granular coal and biomass mixtures under low- to high-stress conditions. The triaxial compression tests are performed on samples of  $230 \times 200$  mesh size and include measurement of axial and volumetric strains. Continuous measurements of permeability and pore volume change are recorded during triaxial deformation together with pre- and postdeformation measurements of particle size distributions. The following conclusions are drawn:

1. Comparison of the mechanical data for all sample types shows that the coal is strongest and the biomass is weakest of all mixtures. Confining stress has a significant effect on deformation. Deformation is dominated by strain hardening and compaction for all samples.
2. Strain hardening is desired for the design of feed system because it will allow applying more stress on the feed which will help to resist the flow of fluid from the gasifier.
3. Because of the low critical strength of all samples grain breakage occurs throughout all experiments—this has a significant effect on all other processes. Grain breakage increases with increasing stress.
4. Deformation in the post failure regime for all sample mixtures follows the CAP model.
5. Permeability reduction is a function of grain breakage, grain size distribution, porosity, deviatoric stress, and it is significantly influenced by confining stress in all sample types.
6. The Kozeny–Carman model cannot correctly predict the permeability loss as it does not consider the grain breakage effect.
7. A new permeability–porosity model is developed to account for the large observed change in permeability with only modest changes in porosity. This model accommodates failure-based reduction in grain size. This is specifically developed to characterize the evolution of permeability under conditions of hydrostatic (isotropic) and deviatoric stress for granular media. This model reveals the reason for the apparently higher-order dependence on porosity change embodied in the

porosity exponent  $\alpha$ . This illustrates that the reduction in permeability is controlled principally by the change in the grain size distribution rather than porosity above critical stresses. Model predictions are consistent with experimental results; however, minor differences are observed between observations and predictions since the weighted harmonic mean grain size slightly under predicts magnitude of the grain-size exponent  $\beta$ .

8. The proposed model results are meaningful for the design of lock-bridge feeders. The further study is warranted in order to come up with predictive models that can be used to obtain the back flow rate and ultimate material strength which are critical engineering parameters for the success of a feeder.

## ■ AUTHOR INFORMATION

### Corresponding Author

\*E-mail: divya.chandra@outlook.com. Phone: 814.865.2225.

### Notes

The authors declare no competing financial interest.

## ■ ACKNOWLEDGMENTS

We have benefitted from discussions with Chris Marone, Hiroko Kitajima, and Marco Scuderi. We thank Shugang Wang, Rohan Belvalkar, Tom McGuire, Brett Carpenter, Bryan Kaproth, Steve Swavely, Michael Disabb Miller, and Julie Anderson for their support. This work is as a result of support from the DOE through the National Energy Technology Laboratory. This support is gratefully acknowledged.

## ■ REFERENCES

- (1) Frey, H. C.; Rubin, E. S. *Environ. Sci. Technol.* **1992**, *26*, 1982–1990.
- (2) Lombardi, L. *Energy Convers. Manage.* **2003**, *44*, 93–108.
- (3) Sprouse, K.; Schuman, M. *AIChE J.* **1983**, *29*, 1000–1007.
- (4) Mann, M.; Spath, P. *Clean Technol. Environ. Pol.* **2001**, *3*, 81–91.
- (5) Mathews, J. P.; Eser, S.; Hatcher, P. G.; Scaroni, A. W. *Image (Rochester, N.Y.)* **2007**, *25*, 145–152.
- (6) Schutjens, P.; Hanssen, T.; Hettema, M.; Merour, J.; J. Ph. de Bree, J. C. G. H.; In *Compaction-induced porosity/permeability reduction in sandstone reservoirs*; Society of Petroleum Engineers: New Orleans, Louisiana, 2001.
- (7) Yale, D.; Crawford, B. In *Plasticity and permeability in carbonates: dependence on stress path and porosity*; Society of Petroleum Engineers: Trondheim, Norway, 1998.
- (8) Wong, T.; David, C.; Zhu, W. *J. Geophys. Res.* **1997**, *102*, 3009–3025.
- (9) Zhu, W.; Wong, T. *Geophys. Res.* **1997**, *102*, 3027–2041.
- (10) Menéndez, B.; Zhu, W.; Wong, T. F. *J. Struct. Geol.* **1996**, *18*, 1–16.
- (11) Karner, S. L.; Chester, J. S.; Chester, F. M.; Kronenberg, A. K.; Hajash, A., Jr. *AAPG Bull.* **2005**, *89*, 603.
- (12) Zoback, M. D.; Byerlee, J. D. *Am. Assoc. Pet. Geol. Bull.* **1976**, *60*, 1531–1542.
- (13) Kitajima, H. Evolution of frictional behavior of punchbowl fault gouges sheared at seismic slip rates and mechanical and hydraulic properties of Nankai trough accretionary prism sediments deformed along different loading paths. Doctoral dissertation, Texas A&M University, 2010.
- (14) Holt, R.; Kjølås, J.; Larsen, I.; Li, L.; Gotusso Pillitteri, A.; Sønstebo, E. *Int. J. Rock Mech. Mining Sci.* **2005**, *42*, 985–995.
- (15) Mogi, K. *Tectonophysics* **1972**, *13*, 541–568.
- (16) Holtz, R. D.; Kovacs, W. D. *New Jersey* **1981**, 342.
- (17) Petch, N. *J. Iron Steel Inst* **1953**, *174*, 25–28.
- (18) Hagin, P. N.; Zoback, M. D. *Geophysics* **2004**, *69*, 742.
- (19) David, C.; Wong, T. F.; Zhu, W.; Zhang, J. *Pure Appl. Geophys.* **1994**, *143*, 425–456.
- (20) Chapuis, R. *Can. Geotech. J.* **2004**, *41*, 787–795.
- (21) Chapuis, R. P.; Contant, A.; Baass, K. A. *Can. Geotech. J.* **1996**, *33*, 168–176.
- (22) Abbas, A.; Nobbs, D.; Romagnoli, J. A. *Knowledge Creation Diff. Util.* **2006**, *13*, 349–356.
- (23) Piggott, A. R.; Elsworth, D. *J. Geophys. Res.* **1992**, *97*, 2085–2093.
- (24) Piggott, A. R.; Elsworth, D. *Geophys. Res. Lett.* **1993**, *20*, 1387–1390.
- (25) Cardwell, W.; Parsons, R. *Trans. AIME* **1945**, *160*, 34–42.
- (26) Bear, J. *Dynamics of fluids in porous media*; Dover publications, 1988.

## ■ NOTE ADDED AFTER ASAP PUBLICATION

This paper published August 17, 2012 with an incorrect reference 13. The correct version published August 23, 2012.